Journal of Materials Chemistry A



PAPER

View Article Online



Cite this: J. Mater. Chem. A, 2024, 12,

Electrochemical control over stoichiometry via cation intercalation into Chevrel-phase sulphides $(Cu_xMo_6S_8, x = 1-3)^{\dagger}$

Kabian A. Ritter, ab Konstantina G. Mason, Suxuen Yew, Joseph T. Perryman, October Jessica C. Ortiz-Rodríguez, Da Nicholas R. Singstock, D*d Brian A. Wuille Bille, *a Charles B. Musgrave*d and Jesús M. Velázquez (1)**ab

This work presents a systematic investigation of the electrochemical intercalation of aqueous copper cations into the Chevrel phase (CP) Mo_6S_8 and its effect on the host's electronic and structural characteristics as a function of stoichiometry. The electrochemical potentials at which copper intercalates into the CP Mo_6S_8 host in 1 M $CuSO_4$ were identified for $Cu_xMo_6S_8$ (x=1–3) as 0.23 V, 0.11 V, and 0.055 V (vs. Cu/Cu²⁺) for Cu₁Mo₆S₈, Cu₂Mo₆S₈, and Cu₃Mo₆S₈, respectively, and correlated via ex situ PXRD to stoichiometric content. Potentials were also identified that yield non-stoichiometric phases with traceable Cu content-dependent structural changes. Ab initio DFT calculations were performed to probe thermodynamic stability of Cu_xMo₆S₈ CP compositions and the metal-tosemiconductor transitions as a function of copper content. Lastly, we demonstrate that the SK-pre-edge intensity is a successful probe for intercalant content: as copper equivalents increase, so does charge transfer to the partially occupied S 3p orbitals, resulting in a decrease in the pre-edge intensity corresponding to the excitation of a S 1s-to-3p/Mo 4d hybridized orbital.

Received 28th November 2023 Accepted 7th February 2024

DOI: 10.1039/d3ta07333e

rsc.li/materials-a

Introduction

The increase in energy demand due to rapid population growth has sparked interest in developing new energy storage and conversion technologies that circumvent environmental and health impacts associated with the use of fossil fuels. 1-3 Despite the promise of alternative green energy technologies such as solar and wind, 1,4-6 significant limitations with energy storage and conversion capabilities prevent the efficient shifting of energy usage during peak demand hours.7 To address this intermittency problem, we need to develop materials that can store energy in the form of vectors which can be readily applied on-demand, preferably, by exploiting existing infrastructure capabilities. These vectors are either electric potential energy (in the form of ions) or chemical energy (in covalent bonds). A candidate bifunctional material is the Chevrel phase, an inorganic solid composed of a system of interconnected clusters

In particular, Chevrel phase (CP) sulphides have historically shown promise as potential state-of-the-art mono and multivalent battery cathode materials given their ability to intercalate/ deintercalate metals such as Mg²⁺, 15-18 Al³⁺, 19 Cd²⁺, 20 Ni²⁺, 21 Zn²⁺, ²²⁻²⁴ Li⁺, ²⁵ and Cu⁺, ^{17,26-28} (Fig. 1a). CPs have also shown promising electrocatalytic activity for various energy conversion reactions, such as the CO₂ reduction reaction (CO₂RR), the hydrogen evolution reaction (HER) and the nitrogen reduction reaction (NRR). 13,26,29 However, many gaps remain in understanding the intercalation behaviour of metals into the CP

with the general formula $M_xMo_6T_8$ (M = transition or alkali metal, T = S, Se, or Te) (Fig. 1c). The binary Chevrel phase, Mo₆T₈, is metastable due to the partially filled p orbitals of the chalcogens that are stabilized by insertion of electron donating metal cations.8-11 The metastability of the binary phase coupled with the cavities and channels formed by the alignment of the clusters allows for the intercalation/deintercalation of metal ions (Fig. 1b).12 The geometric differences between cavities displayed in Fig. 1b allows a preferred arrangement of cations within the structure. Large cations (broadly defined as having radii >1 Å) tend to prefer hexahedral coordination in the centre of Site 1 (purple) while smaller cations (radii <1 Å) prefer tetrahedral coordination in off-centred positions of Site 1.13,14 At higher stoichiometric equivalents (x > 1), both small and large cations commonly occupy Site 2 (orange).13 Its compositional flexibility makes the Chevrel phase an excellent canvas for the study of the fundamental structure-function correlations.

^aDepartment of Chemistry, University of California, One Shields Avenue, Davis, California 95616, USA. E-mail: jevelazquez@ucdavis.edu

^bEnergy Systems, Energy and Efficiency Institute, University of California, 1605 Tilia St #100, Davis, California 95616, USA

Department of Chemical Engineering, Stanford University, 381 North-South Mall, Stauffer II, Stanford, California 94305, USA

^dDepartment of Chemical and Biological Engineering, University of Colorado Boulder, Boulder, Colorado 80303, USA

available. See DOI: † Electronic supplementary information (ESI) https://doi.org/10.1039/d3ta07333e

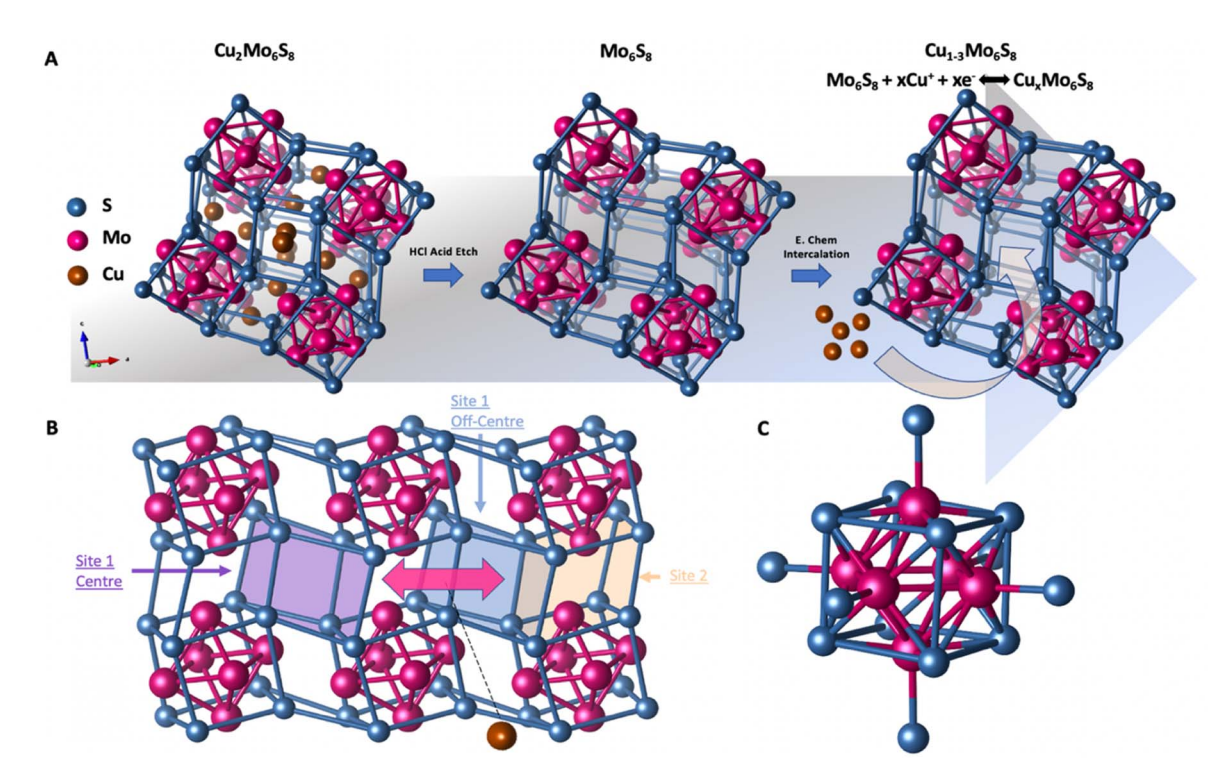


Fig. 1 (A) Schematic of synthesis of $Cu_xMo_6S_8$ (x=1-3) phases via electrochemical intercalation. From left to right: $Cu_2Mo_6S_8$ starting material synthesized via microwave-assisted solid-state methods (left), binary CP after acid etching of $Cu_2Mo_6S_8$ (centre), and schematic depicting control over stoichiometric Cu content within the CP host via electrochemical methods with accompanied chemical equation (right). (B) Depiction of the CP cavity network arising from repeated Mo_6S_8 clusters creating cavities with different coordination environments, Site 1 Centre (purple), Site 1 Off-Centre, and Site 2 (orange), that can accommodate metal cations. Note that Site 1 Centre and Site 1 Off-Centre are equivalent cavities and are distinguished solely by cation occupation coordination as previously described. (C) An Mo_6S_8 cluster unit showing six additional axial bonds between Mo (pink) and S (blue) that link adjacent clusters together.

framework, especially in aqueous electrolytes, which represent a cost-effective alternative to toxic and volatile organic electrolytes used in mainstream lithium-ion batteries (LIB) and in many energy conversion reactions such as $\rm CO_2RR$ and $\rm NRR.^{30,31}$

In this work, we report the sequential electrochemical intercalation of transition metal cations into the Chevrel phase framework and the effects on atomic and electronic structures. Herein we focus on the intercalation and deintercalation of Cu, due to its high mobility,12 promising catalytic activity,26 and general lack of understanding of its role in determining the conduction properties of Cu_xMo₆S₈. Through a combination of powder X-ray diffraction (PXRD), X-ray photoelectron spectroscopy (XPS), and X-ray absorption near-edge structure (XANES), each electrochemical potential was experimentally correlated to a stoichiometric copper content ($Cu_xMo_6S_8$, x = 1-3). In addition, Density Functional Theory (DFT) calculations and density of states (DOS) of the $Cu_xMo_6S_8$ intercalated structures provide insight into their stability and bandgap shifts that result as a function of the Cu content in the Cu_xMo₆S₈ system. The DFT calculations include Cu₄Mo₆S₈ to consider the entire range of Cu intercalated stoichiometries that the CP may host to better understand the synthesizability challenges the Cu₄Mo₆S₈ phase presents. Finally, we used S K-edge XANES to monitor intercalant presence and its effect on the host system's electronic properties.

Within the broad compositional space of CPs, $\mathrm{Cu_2Mo_6S_8}$ has proven to be a promising cathode material as well as an active electrocatalyst for energy conversion reactions. However, there is not a systematic study that deconvolutes the structural changes that arise from all the electrochemically intercalated copper stoichiometries ($\mathrm{Cu_xMo_6S_8}$, x=1–4) in aqueous media. In addition, the Cu–Mo–S compositional space holds promise due to a theoretically predicted metal-to-semiconductor transition in the CP system as a function of stoichiometry and position of the Cu intercalant within the lattice.

Experimental

Materials

MoS₂ powder (99%, ~325 mesh), Cu powder (99.995%, ~100 mesh), and graphite powder (99% purity) were used as purchased from Alfa Aesar. Mo powder (99.99%, ~100 mesh), Cu foil (thickness 0.25 mm, 99.98%) CuSO₄·5H₂O (98.0%), concentrated H₂SO₄ acid (ACS grade) were used as purchased from Sigma-Aldrich. Fused quartz tubes (2 mm thick) were purchased from AdValue Technology and made into round-bottom tubes with an in-house oxy-hydrogen torch. 3MTM Electroplating Tape 470 was used as purchased. All divalent salt solutions were prepared with 18.2 MΩ cm⁻¹ water from a Thermo-Fisher Barnstead E-pure® purification system and did not require pre-electrolysis treatment.

Material synthesis

CP sulphide catalysts were prepared according to previously reported solid-state synthesis methods. 18,26,32 In summary, stoichiometric amounts of the necessary precursors were weighed out in a N2 glovebox to achieve Cu2Mo6S8 and pressed into a pellet that was then sealed in a quartz tube with alumina wool and graphite before being placed in a microwave for 10 min at approximately 1000 °C. Following the microwaveassisted synthesis of Cu₂Mo₆S₈, the copper was etched out of the material through immersion in 14 M HCl for 48 hours, as seen in Fig. S8.† All electrochemical intercalation experiments used a custom designed three-electrode single compartment beaker-style cell (Fig. S1f†). The working electrode (WE) was an ink comprised of the previously synthesized Mo₆S₈ powder, carbon black, and polytetrafluoroethylene (PTFE) dispersed in isopropanol (IPA) and 100 µL was drop-cast onto a masked glassy carbon (GC) support. A mask of electroplaters (3 M) tape was used (Fig. S1†) to limit exposure of the GC support to surrounding electrolyte. 100 µL of the CP ink was drop-cast onto the exposed window of the GC electrode. Strips of Cu foil were used as the counter (CE) and reference (RE) electrodes, respectively. These foils were encased in insulating Teflon tape to prevent electrodes from touching and short-circuiting during experiments (Fig. S1c†). All electrochemical analyses were performed using a Bio-Logic VSP-300 potentiostat.

The Cu_xMo₆S₈ intercalated Chevrel-phase (I-CP) materials were obtained by the electrochemical reduction of Cu²⁺ in 1 M $CuSO_4$ electrolyte solution at pH \sim 3, with a drop-cast GC-Mo₆S₈ WE. Electrochemical experiments were performed under Ar and carried out at room temperature. All values are reported as $E_{\rm WE}$ (V vs. Cu/Cu²⁺). To acquire each of the stoichiometric samples of $Cu_xMo_6S_8$, where x = 1-3, the starting potential was 0.30 V vs. Cu/Cu²⁺ and scan rate was 0.050 mV s⁻¹ for all experiments. For cyclic voltammetry (CV) experiments, the potential was cathodically swept to 0 V vs. Cu/Cu^{2+} and -0.070 V vs. Cu/Cu^{2+} to achieve Cu₂Mo₆S₈ and Cu₃Mo₆S₈, respectively. Background LSV scans in the same potential window were taken for bare GC electrodes and for GC electrodes with ink but no CP (Fig. S6†).

Structural and electronic characterization

Crystal structures and phase purity of as-synthesized CPs and intercalated species were analyzed via PXRD using a Bruker D8 Advance diffractometer with Cu K_{α} radiation (1.5406 Å). The obtained powder diffraction patterns were compared to literature patterns from the Inorganic Crystal Structure Database (ICSD). Morphology of synthesized CPs before and after the etching process was evaluated via scanning electron microscopy (SEM) using a FEI Nova NanoSEM 430 (Hillsboro, Or). Bulk composition of I-CP materials was also evaluated via energydispersive X-ray spectroscopy (EDX) using a FEI Scios Dual Beam FIB/SEM with an Oxford EDX detector. Surface composition was investigated using a Kratos Supra Axis X-ray Photoelectron Spectrometer (Shimadzu corporation) with a monochromatic Al K_a source (1486.6 eV). Electronic information was obtained through X-ray absorption spectroscopy (XAS) at Stanford Synchrotron Radiation Lightsource (SSRL)

beamlines 4-1 (vertically collimating, flat, bent, 1.0 m, Si, Rhcoated) and 4-3 (vertically collimating, flat, bent, 1.0 m, bare Si).

Computational methods

DFT calculations were performed using the Vienna Ab initio Simulation Package (VASP).33 Ground state structures and total energies were computed with the Strongly Constrained and Appropriately Normed (SCAN)34 meta-GGA (Generalized Gradient Approximation) density functional. The DOS of all Cu intercalated CPs, and the band gap of Cu₄Mo₆S₈ were calculated at SCAN converged structures using the Heyd-Scuseria-Ernzerhof hybrid-density functional with 20% Hartree-Fock screening (HSE06).35 All calculations were performed with PAW-PBE pseudopotentials with kinetic energy terms, a plane wave energy cut-off of 520 eV and a Γ -centered k-point grid with a density of 1200/N, where N is the number of atoms in the unit cell. Formation enthalpies (ΔH_f) were calculated using:

$$\Delta H_{
m f} = E_{
m CP} - \sum_{
m el}^{
m atoms} E_{
m ref}(
m el), \,\,$$
 where $E_{
m CP}$ is the total energy of the

respective CP and $E_{ref}(el)$ is the total energy per atom of the reference element, which is summed over all atoms in the unit cell. $\Delta H_{\rm f}$ values for each $Cu_x Mo_6 S_8$ (x = 1-4) intercalated structure under applied potential (V) were calculated using the Nernst equation: $\Delta H_{f,V}(V) = \Delta H_f - xFV$, where x is the number of electrons (i.e., number of Cu⁺ intercalants) relative to the Cu⁰ and Mo_6S_8 reference phases and F is Faraday's constant (1 eV).

Results and discussion

Stoichiometric control over the intercalation of Cu ions into the Mo₆S₈ host was achieved by controlling the electrochemical potential of the working electrode (WE). In principle, the electrochemical intercalation of Cu⁺ (after its reduction from the CuSO₄ electrolyte) is expected to follow a multi-step process similar to that of other multivalent and monovalent species, in which the insertion occurs sequentially:16,17,28

$$Mo_6S_8 + Cu^+ + e^- \leftrightarrow Cu_1Mo_6S_8$$
 (1)

$$Cu_1Mo_6S_8 + Cu^+ + e^- \leftrightarrow Cu_2Mo_6S_8$$
 (2)

$$Cu_2Mo_6S_8 + Cu^+ + e^- \leftrightarrow Cu_3Mo_6S_8 \tag{3}$$

$$Cu_3Mo_6S_8 + Cu^+ + e^- \leftrightarrow Cu_4Mo_6S_8$$
 (4)

Thus, a reductive current response for each stoichiometric intercalation of Cu ions into the structure was anticipated. Inspection of the cyclic voltammogram in Fig. 2a shows several cathodic waves are present in the reductive sweep. Contrary to our expectations, results of such experiments demonstrated that each reductive wave (P-1-4) in Fig. 2a is not directly correlated to the intercalation of a single stoichiometric equivalents of Cu in the system, as has been seen in other CP intercalation studies with different cations. 16,17,19,23 Fig. 2a reveals that reduction currents at 0.23 V (1) and 0.11 V (P-3) correlate to the formation of Cu₁Mo₆S₈ and Cu₂Mo₆S₈, respectively, as shown by their diffractograms (Fig. 2b and c). The cathodic wave centered

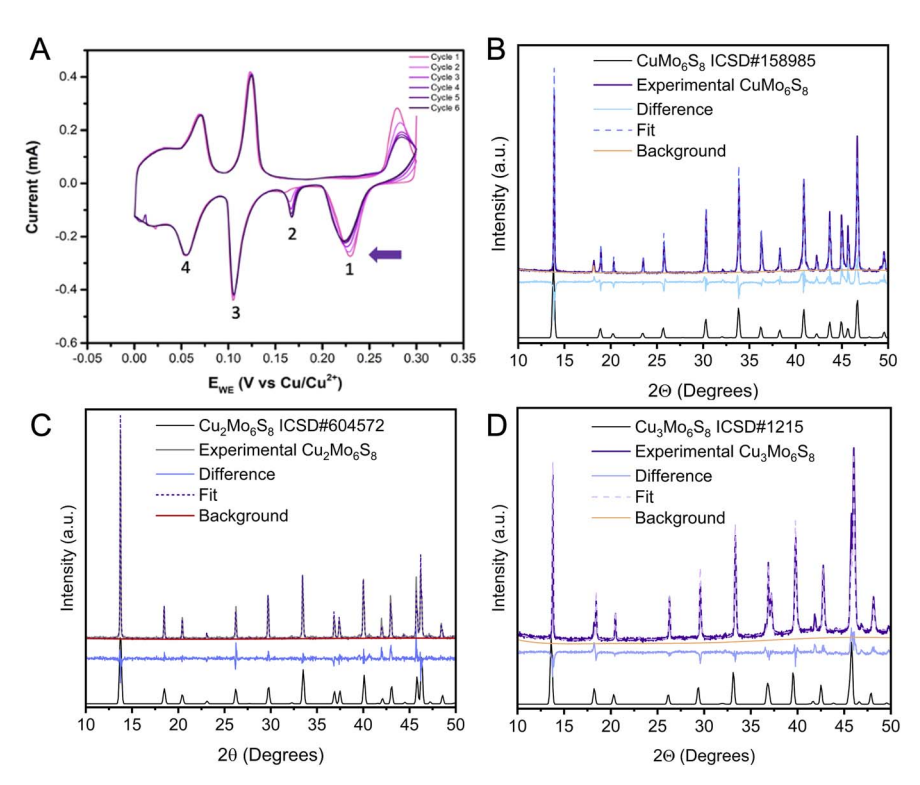


Fig. 2 (A) Cyclic voltammogram (CV) of binary Mo_6S_8 deposited on GC electrode, used as WE for electrochemical intercalation/deintercalation in 1 M CuSO₄ solution. Each cathodic wave is numbered and the arrow indicates the scanning direction. (B)–(D) PXRD of experimentally synthesized, electrochemically intercalated $Cu_xMo_6S_8$ overlaid with reference patterns from the Inorganic Crystal Structure Database (ICSD) for $Cu_1Mo_6S_8$ (C), $Cu_2Mo_6S_8$ (D), and $Cu_3Mo_6S_8$ (E).

at 0.05 V corresponds to the synthesis of $\mathrm{Cu_3Mo_6S_8}$. As seen in Fig. 2b–d, the increase in copper content induces an expansion of the lattice, which is evidenced by a shift of the characteristic CP reflection of the (101) plane to lower 2θ . There is also clear migration of further reflections as Cu content increases in the CP host (Fig. S5†). This was confirmed with Rietveld refinement analysis of the $\mathrm{Cu_1Mo_6S_8}$, $\mathrm{Cu_2Mo_6S_8}$, and $\mathrm{Cu_3Mo_6S_8}$ diffractograms, in which the volume of the unit cell expands as additional Cu equivalents are intercalated (Table S1†). In addition to the $\mathrm{Cu_xMo_6S_8}$ (x=1,2, or 3) phases, one other reductive signal was observed at 0.17 V (P-2). We confirmed that the reductive wave P-2 can be attributed to the non-stoichiometric intercalation of Cu to form $\mathrm{Cu_{1.8}Mo_6S_8}$ (Fig. S3†).

Fig. 2a shows minimal (\sim 15 mV) peak-to-peak separation between the reductive and oxidative current responses for P-3 and P-4 indicating the reversible nature of intercalation of the Cu species into/from the CP host material, consistent with the reported increase in chemical diffusivity of Cu ions with increasing copper content.²⁸ Comparatively, the separation between the cathodic and anodic waves in the potential P-1 equals \sim 50 mV, denoting lower reversibility than P-3 and P-4.³⁷ The slight shift in potentials as cycle number increases for the deintercalation of Cu $^+$ from Cu $_1$ Mo $_6$ S $_8$ back to binary Mo $_6$ S $_8$ at 0.28 V is evidence of Cu trapping within the CP host's cavities. This behavior has been widely reported for multiple metals in the CP system.^{14,16,17,19,23} Trapping of metal ions can lead to slight overpotentials needed to intercalate a Cu ion into the CP host as cycles increase, as observed in P-1. These results and

analysis are consistent with work from Saha et al. who proposed that the differences in current response position between cycles result from different chemical potentials that arise from compositional change (i.e., $Mo_6S_8 \rightarrow M_xMo_6S_8$) due to trapping of metal intercalants.38 The intercalation potential required to achieve Cu₃Mo₆S₈ is slightly lower than the Cu/Cu²⁺ redox potential (Fig. S4†) and approaches the region where both the complete reduction to metallic Cu and HER (\sim -0.20 V) are competing reactions, according to the Pourbaix diagram for Cu (Fig. S2†),36 unlike the milder potential ranges for Cu₁Mo₆S₈ and Cu₂Mo₆S₈ electrosynthesis. As a result, co-plating of Cu metal in the more negative potential ranges is more thermodynamically favored than intercalation into the CP host, as is indicated by a nucleation loop in the CV (Fig. S4a†).21 This nucleation loop in cyclic voltammetry is believed to arise from an overpotential for the deposition of a metal on the electrode. This is followed by the subsequent growth of the metallic layer at its redox potential.39 It was also observed that Cu metal tended to plate on exposed areas of the GC WE without any CP deposited at these negative potentials. To prevent co-plating during the electrosynthesis of Cu₃Mo₆S₈, we limited exposed GC surface area (Fig. S1c and f†) and carefully selected cut-off potentials. This was done by incrementally decreasing (by -0.01 V) the potential window and analyzing samples ex situ to identify the exact potential where Cu metal plating occurred. Energy dispersive X-ray spectroscopy analysis confirms uniform distribution of Cu (Fig. S7†); atomic percentages of Cu in the intercalated samples agree well with the expected atomic

percentages for stoichiometric Cu₁Mo₆S₈ (Cu = 6.7%), $Cu_2Mo_6S_8$ (Cu = 12.5%), and $Cu_3Mo_6S_8$ (Cu = 17.6%), respectively.

Electronic structure characterization

Each I-CP sample shows the presence of Cu in the CP host system at an oxidation state that approximates Cu(I) for Cu₁Mo₆S₈ (Fig. 3a), Cu₂Mo₆S₈ (Fig. 3b), and a mixture of both Cu(I) and Cu(II) for Cu₃Mo₆S₈ (Fig. 3c), all of which agree well with literature values.34,35 The presence of Cu(II) on the surface of Cu₃Mo₆S₈ is due to residual CuSO₄ as seen in the S 2p XPS data in Fig. S9.† It is noted that residual sulfate electrolyte was observed in multiple samples at binding energies ca. 168 eV. This residual electrolyte was randomly distributed throughout analysis sites despite several washes with high-purity water. The need to maintain the mechanical integrity of the samples prevented more vigorous cleaning that would have ensured complete removal. All samples were sputtered with Ar⁺ to avoid analyzing potential native oxides on the surface when samples were exposed to air. Work published by Levi and Biesinger indicates the Cu(1) oxidation state in Cu₂Mo₆S₈, using XPS, which closely matches literature values for Cu2S.40 To observe the effect that stoichiometric Cu intercalants had on CP electronic structure, X-ray absorption near-edge spectroscopy (XANES) was carried out. Fig. 4 shows overlaid data of the sulphur K-edge region for the binary CP (black), Cu₁Mo₆S₈ (purple), Cu₂Mo₆S₈ (red), and Cu₃Mo₆S₈ (blue) I-CPs. As more Cu is introduced into the system, there is a progressive depression of the SK-pre-edge feature at 2471 eV. This depression indicates a filling of unoccupied orbitals of the sulphur via donated electron density from the Cu intercalant. With an increase in the equivalents of guest metal, the partially empty S 3p orbitals, hybridized with Mo 4d orbitals, become progressively more occupied, thereby decreasing the pre-edge feature intensity.24,40 It is expected that as four stoichiometric equivalents of Cu are intercalated into the system (Cu₄Mo₆S₈) the previously electron deficient binary cluster (Mo₆S₈) would have satisfied its theoretically achievable maximum number of valence electrons in bonding orbitals and a full depression of the pre-edge feature would occur.10

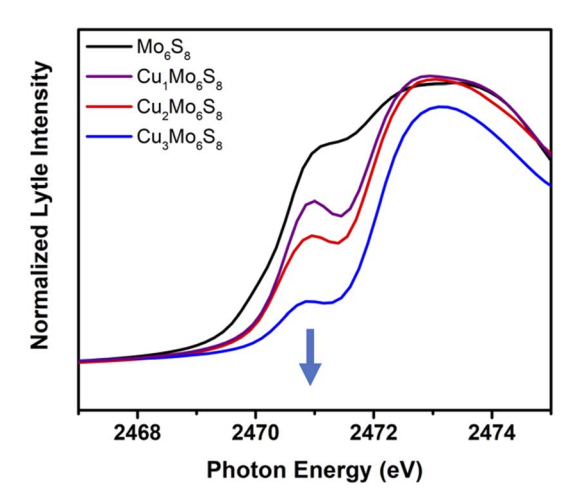


Fig. 4 XANES spectra showing SK-pre-edge data for binary CP (Mo_6S_8) , the systematic decrease in the S K-pre-edge feature as a function of Cu content. The arrow indicates the pre-edge region and the direction of the depression as a function Cu content.

In comparison with works where Li⁺, Na⁺, Mg²⁺, Al³⁺, and Zn²⁺ were intercalated into the CP sulphide framework, 15,17,19,22-25,38 these metals show improved kinetics as a function of cycle increase (e.g., a shift to lower overpotentials as cycles increased). CVs carried out in the potential window for $Cu_xMo_6S_8$; x = 1 (eqn (1)) and x = 2 (eqn (2)), show potential shifts when one or two cation equivalents are intercalated. However, the current remains largely unchanged following further intercalations. Figure S4† shows that as Cu_{x>2}Mo₆S₈ is achieved, there is a shift to lower overpotentials for intercalation/deintercalation as cycles increase, indicating an increase in ionic conductivity in the system. This result aligns with the findings of Levi et al. that as the number of Cu equivalents surpasses x = 2, the repulsion effects between cations cause a migration to Site 2 and an increase in the solidstate ion conduction.14

Thermodynamic stability and density of states modeling

As previously discussed, one of the motivations for exploring the Cu-Mo-S compositional space is to investigate

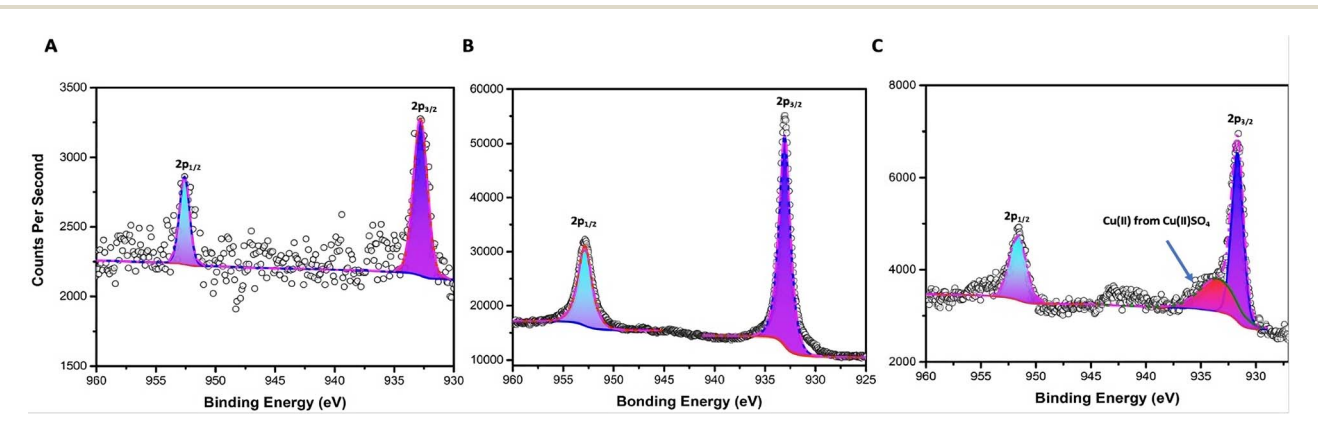


Fig. 3 XPS spectra showing the Cu 2p signal for post-etch scans for experimentally intercalated (A) $Cu_1Mo_6S_8$, (B) $Cu_2Mo_6S_8$, and (C) $Cu_3Mo_6S_8$. Residual Cu(II)SO₄ electrolyte that could not be removed by washing in panel C is labelled for clarity.

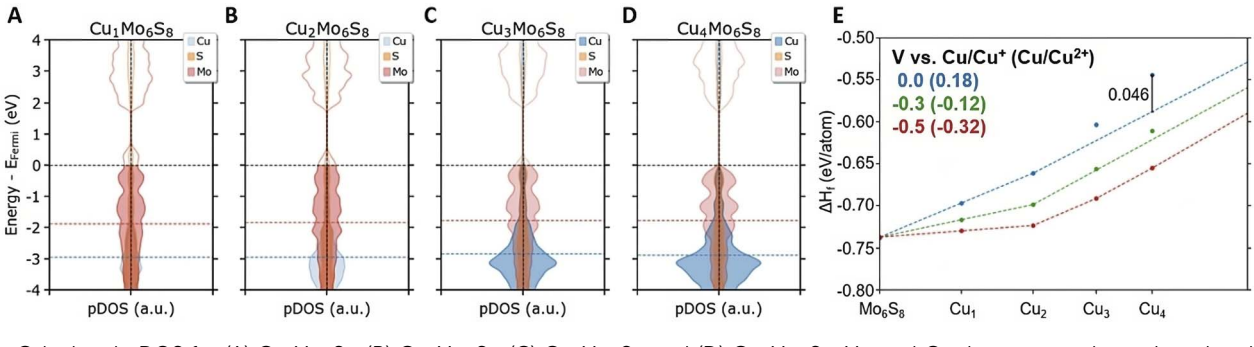


Fig. 5 Calculated pDOS for (A) $Cu_1Mo_6S_8$, (B) $Cu_2Mo_6S_8$, (C) $Cu_3Mo_6S_8$, and (D) $Cu_4Mo_6S_8$. Mo and Cu d-states are shown in red and blue, respectively, and S p-states are shown in orange. The dashed red and blue lines indicate the d-band centers for Mo and Cu, respectively. The convex hulls of $Cu_xMo_6S_8$ (E) shows the stability of competing phases at 0.0 V, -0.3 V and -0.5 V vs. Cu/Cu^+ . Materials on the convex hull (dashed lines) are stable. Bias vs. Cu/Cu^{2+} is indicated in parenthesis. Full compositions are omitted for $Cu_{1-4}Mo_6S_8$ phases (e.g., $Cu_1 = Cu_1Mo_6S_8$).

a theoretically predicted metal-to-semiconducting bandgap transition as a function of Cu content within the CP sulphide system. To validate this prediction, we calculated orbitalprojected density of states (pDOS) using DFT with the highfidelity HSE06 functional. Fig. 5a-d show the pDOS for Cu₁₋ ₄Mo₆S₈. As the Cu stoichiometry increases, the density of Cu dstates near -3 eV also increases. The Cu d-states donate electron density to the Mo₆ octahedra, thereby populating the Mo conduction band d-states near the Fermi level. These Mo dstates become fully occupied (i.e., valence band states) in Cu₄Mo₆S₈. Consequently, the Cu₄Mo₆S₈ phase is predicted to be semiconducting with a bandgap of 1.61 eV. Our calculations predict that all studied polymorphs of the Cu₄Mo₆S₈ composition are semiconducting with bandgaps of 1.61-1.86 eV. Although theory provides a strong motivation to synthesize Cu₄Mo₆S₈ as a semiconducting CP, this material was not experimentally realized. Fig. 5e shows the convex hull of the $Cu_xMo_6S_8$ phase space, where the ΔH_f of the competing phases are shown relative to their Cu molar content. Materials are included as points, which either fall on the convex hull (dashed line), indicating that they are stable, or above the convex hull, indicating that they are unstable with respect to decomposition into competing phases. Here, a greater distance from the convex hull indicates greater instability. At 0.0 V vs. Cu/Cu⁺ (0.18 V vs. Cu/Cu²⁺), Cu₄Mo₆S₈ lies above the convex hull by 46 meV/atom, indicating that it is metastable (i.e., <65 meV per atom¹³). As a reductive potential is applied, the intercalation reduction reactions (eqn (1)-(4)) become more favourable due to the stabilization of electrons in the higher Cu-content CPs. Consequently, at reducing biases of -0.3 V and -0.5 V vs. Cu/Cu⁺ $(-0.12 \text{ and } -0.32 \text{ V } \text{vs. Cu/Cu}^{2+})$, the Cu₃Mo₆S₈ and Cu₄Mo₆S₈ phases are stabilized onto the convex hull, respectively. These results predict that these phases are synthesizable under reducing conditions. Conversely, at an oxidative potential above 0.1 V vs. Cu/Cu^+ (0.28 V vs. Cu/Cu^{2+}) the $Cu_1Mo_6S_8$ and Cu₂Mo₆S₈ phases are destabilized and come off the convex hull. This agrees with the experimental CV, which indicates that the Cu₁Mo₆S₈ and Cu₂Mo₆S₈ phases form between 0.25 and 0.10 V vs. Cu/Cu²⁺ and that Cu₃Mo₆S₈ forms at reductive potentials below $-0.05~\mbox{V}$ vs. $\mbox{Cu/Cu}^{2^+}.$ However, plating of copper cations

will occur at reductive potentials below 0.0 V νs . Cu/Cu²⁺ and hydrogen evolution will occur in aqueous electrolytes below -0.34 V νs . Cu/Cu²⁺. The competition with copper plating and hydrogen evolution at the electrochemical conditions necessary to stabilize Cu₄Mo₆S₈ limits the synthetic accessibility of this material.

Previous work reports the successful synthesis of $Cu_4Mo_6S_8$ with *in situ* PXRD while applying a negative bias to the system. However, our *ex situ* PXRD (see Fig. S10†) characterization under the same experimental conditions only indicates the successful synthesis of $Cu_3Mo_6S_8$. This suggests that an electrochemical bias is necessary to maintain $Cu_4Mo_6S_8$, and that once this bias is removed the CP loses one Cu atom per formula unit *via* deintercalation to yield the $Cu_3Mo_6S_8$ phase. To our knowledge, there are also no reports of $Cu_4Mo_6S_8$ being synthesized *via* solid-state methods without an applied potential. A promising strategy to corroborate the predicted metal-to-semiconductor transition for the $Cu_1-_4Mo_6S_8$ system is to characterize $Cu_4Mo_6S_8$ *in situ* under reducing bias, which is the subject of a follow-up study to this work.

Conclusion

In conclusion, we have experimentally determined electropotentials for successive Cu intercalation/ deintercalation into/out of the binary Mo₆S₈ framework up to Cu₃Mo₆S₈ in aqueous environments. Additionally, we have carried out a systematic electrochemical study correlating reductive intercalation potentials to stoichiometric Cu content in the Chevrel-phase sulphides using PXRD and EDX. Lastly, we were able to probe the charge transfer and surface electronic structure, through XANES and XPS allowing us to observe Cu oxidation state and its effect on the host structure electronic properties as a function of increasing intercalant content. Using XANES we monitored the progressive depression of the SK-preedge feature as a function of metal intercalant, which indicates a filling of the conduction band states in close agreement with computation. This could serve as a tool for future work in the field to observe intercalant presence and effect on host materials as a function of orbital populations and the effects of

different intercalant stoichiometries on CO2RR in aqueous environments.

While we report successful aqueous electrochemical intercalation using potentiometric methods up to Cu₃Mo₆S₈, we acknowledge limitations due to co-plating reactions at more negative potentials as previously discussed. Thus, complementary work using alternative electrochemical methods (e.g., in situ galvanostatic and pulsed intercalation) are planned to synthesize the theoretically achievable Cu₄Mo₆S₈ phase to observe full sulphur K pre-edge depression and in situ XRD peak evolution, and to probe possible photoactivity stemming from semiconducting behavior. Future work to confirm the hypothesis of Cu cavity migration as a function of stoichiometry and oxidation state change includes in situ PXRD correlated to pair distribution function (PDF) analysis allowing us to extract additional structural information. This work provides fundamental insights into cation intercalation behavior and its subsequent electronic and structural effects within CP sulphides, which are presently promising candidates in the multivalent cathode research space considering discoveries over the past decade. The findings in this work can help guide the field to discovering and understanding new intercalated CP compositional spaces for energy storage and other electronic applications.

Author contributions

Kabian Ritter made contributions through material synthesis, electrochemical analysis, analytical chemistry (PXRD, XPS, EDS, and XAS), and manuscript writing. Brian Wuille-Bille made contributions to this work through material analysis (XPS and XAS) and manuscript writing. Suxuen Yew and Nicholas Singstock made contributions through theoretical calculations and manuscript writing. Joseph Perryman, Jessica Ortiz-Rodríguez, and Konstantina Mason made contributions through manuscript writing. Professors Jesús Velázquez and Charles Musgrave supervised the experimental and theoretical calculations as well as the writing of the manuscript.

Conflicts of interest

There are no conflicts to declare.

Acknowledgements

K. A. R. was funded through the UC-HBCU Fellowship from the University of California Office of the President. K. A. R. also acknowledges the Dean's Collaborative Research (DECOR) award through the Engineering Dean's office. K. A. R. also acknowledges Leah Filardi and the Advance Materials Characterization and Testing Laboratory (AMCaT). J. M. V. thanks the University of California, Davis, for start-up funding, as well as support from the Cottrell Scholar program supported by the Research Corporation for Science Advancement (RCSA 26780). J. M. V. acknowledges funding support from the NSF through the Faculty Early Career Development Program (DMR-2044403). JMV also acknowledges funding support from the Camille Dreyfus Teacher Scholar and

Alfred P. Sloan Foundation awards. Use of the Stanford Synchrotron Radiation Lightsource, SLAC National Accelerator Laboratory, is supported by the U.S. Department of Energy, Office of Science, Office of Basic Energy Sciences under Contract No. DE-AC02-76SF00515. XPS analysis at UC Davis was supported by the National Science Foundation (DMR-1828238). C. B. M. and N. R. S. acknowledge support from the National Science Foundation (CBET-2016225). A portion of the research was performed using computational resources sponsored by the Department of Energy's Office of Energy Efficiency and Renewable Energy and located at the National Renewable Energy Laboratory.

References

- 1 Annual Energy Outlook 2022: With Projections to 2050, https:// www.eia.gov/outlooks/aeo/, accessed April 2022.
- 2 C. W. Tessum, D. A. Paolella, S. E. Chambliss, J. S. Apte, J. D. Hill and J. D. Marshall, Sci. Adv., 2021, 7(18), eabf4491.
- 3 M. A. G. Demetillo, A. Navarro, K. K. Knowles, K. P. Fields, J. A. Geddes, C. R. Nowlan, S. J. Janz, L. M. Judd, J. Al-Saadi and K. Sun, Environ. Sci. Technol., 2020, 54(16), 9882-9895.
- 4 F. Creutzig, P. Agoston, J. C. Goldschmidt, G. Luderer, G. Nemet and R. C. Pietzcker, Nat. Energy, 2017, 2(9), 17140.
- 5 E. Kabir, P. Kumar, S. Kumar, A. A. Adelodun and K. H. Kim, Renewable Sustainable Energy Rev., 2018, 82, 894-900.
- 6 X. Lu and M. B. McElroy, Wind Energy Eng. A Handb. Onshore Offshore Wind Turbines, 2017, vol. 5, pp. 51-73.
- 7 P. Denholm, M. O'Connell, G. Brinkman and J. Jorgenson, Tech. Rep., NREL/TP-6A20-65023, 2015, vol. 46.
- 8 L. F. Wan, J. Wright, B. R. Perdue, T. T. Fister, S. Kim and C. A. Apblett, Phys. Chem. Chem. Phys., 2016, 18(26), 17326-17329.
- 9 R. Chevrel, M. Hirrien and M. Sergent, Polyhedron, 1986, 5(1-2), 87-94.
- 10 Ø. Fischer, Appl. Phys., 1978, 16(1), 1-28.
- 11 K. Yvon and A. Paoli, Solid State Commun., 1977, 24(1), 41-
- 12 N. R. Singstock, J. C. Ortiz-Rodríguez, J. T. Perryman, C. Sutton, J. M. Velázquez and C. B. Musgrave, J. Am. Chem. Soc., 2021, 143, 9113-9122.
- 13 N. R. Singstock and C. B. Musgrave, J. Am. Chem. Soc., 2022, 144(28), 12800-12806.
- 14 E. Levi, G. Gershinsky, D. Aurbach, O. Isnard and G. Ceder, Chem. Mater., 2009, 21(7), 1390-1399.
- 15 D. Aurbach, Z. Lu, A. Schechter, Y. Gofer, H. Gizbar, R. Turgeman, Y. Cohen, M. Moshkovich and E. Levi, ChemInform, 2010, 32(3), 724-727.
- 16 D. Muthuraj and S. Mitra, Mater. Res. Bull., 2018, 101(2017),
- 17 S. H. Choi, J. S. Kim, S. G. Woo, W. Cho, S. Y. Choi, J. Choi, K. T. Lee, M. S. Park and Y. J. Kim, ACS Appl. Mater. Interfaces, 2015, 7(12), 7016-7024.
- 18 E. Lancry, E. Levi, Y. Gofer, M. Levi, G. Salitra and D. Aurbach, Chem. Mater., 2004, 16(14), 2832-2838.
- 19 L. Geng, G. Lv, X. Xing and J. Guo, Chem. Mater., 2015, 27(14), 4926-4929.

- 20 J. Barbosa, C. Prestipino, O. J. Hernandez, S. Paofai, C. Dejoie, M. Guilloux-Viry and C. Boulanger, *Inorg. Chem.*, 2019, 58(3), 2158–2168.
- 21 E. Guyot, S. Seghir, J. M. Lecuire, C. Boulanger, M. D. Levi, Y. Shilina, V. Dargel and D. Aurbach, *J. Electrochem. Soc.*, 2013, **160**(3), A420–A425.
- 22 Y. Cheng, L. Luo, L. Zhong, J. Chen, B. Li, W. Wang, S. X. Mao, C. Wang, V. L. Sprenkle and G. Li, ACS Appl. Mater. Interfaces, 2016, 8(22), 13673–13677.
- 23 M. S. Chae, J. W. Heo, S. C. Lim and S. T. Hong, *Inorg. Chem.*, 2016, 55(7), 3294–3301.
- 24 B. Lee, W. J. No and S. H. Oh, J. Power Sources, 2020, 478, 229086.
- 25 M. D. Levi, H. Gizbar, E. Lancry, Y. Gofer, E. Levi and D. Aurbach, *J. Electroanal. Chem.*, 2004, **569**(2), 211–223.
- 26 J. T. Perryman, J. C. Ortiz-Rodríguez, J. W. Jude, F. P. Hyler, R. C. Davis, A. Mehta, A. R. Kulkarni, C. J. Patridge and J. M. Velázquez, *Mater. Horiz.*, 2020, 7(1), 193–202.
- 27 R. Schöllhorn, M. Kümpers, A. Lerf, E. Umlauf and W. Schmidt, *Mater. Res. Bull.*, 1979, 14(8), 1039–1047.
- 28 C. Fischer, E. Gocke, U. Stege and R. Schöllhorn, *J. Solid State Chem.*, 1993, 54–68.
- 29 J. C. Ortiz-Rodríguez, N. R. Singstock, J. T. Perryman, F. P. Hyler, S. J. Jones, A. M. Holder, C. B. Musgrave and J. M. Velázquez, ACS Appl. Mater. Interfaces, 2020, 12(32), 35995–36003.

- 30 F. Murgia, P. Antitomaso, L. Stievano, L. Monconduit and R. Berthelot, *J. Solid State Chem.*, 2016, 242, 151–154.
- 31 J. A. M. Salgado, J. U. Chavarín and D. M. Cruz, *Int. J. Electrochem. Sci.*, 2012, 7(2), 1107–1117.
- 32 E. Levi, A. Mitelman, D. Aurbach and M. Brunelli, *Chem. Mater.*, 2007, **19**(21), 5131–5142.
- 33 G. Kresse and J. Furthmüller, *Phys. Rev. B: Condens. Matter Mater. Phys.*, 1996, **54**(16), 11169–11186.
- 34 J. Sun, A. Ruzsinszky and J. P. Perdew, *Phys. Rev. Lett.*, 2015, 115(3), 036402.
- 35 J. Heyd and G. E. Scuseria, J. Chem. Phys., 2003, 118, 8207.
- 36 M. Pourbaix, Atlas of Chemical and Electrochemical Equilibria in Aqueous Solutions, *Natl. Assoc. Corros. Eng.*, 1974.
- 37 N. Elgrishi, K. J. Rountree, B. D. McCarthy, E. S. Rountree, T. T. Eisenhart and J. L. Dempsey, *J. Chem. Educ.*, 2018, 95(2), 197–206.
- 38 P. Saha, P. H. Jampani, M. K. Datta, D. Hong, C. U. Okoli, A. Manivannan and P. N. Kumta, *J. Phys. Chem. C*, 2015, 119(11), 5771–5782.
- 39 J. Heinze, A. Rasche, M. Pagels and B. Geschke, *J. Phys. Chem. B*, 2007, **111**(5), 989–997.
- 40 M. C. Biesinger, L. W. M. Lau, A. R. Gerson and R. S. C. Smart, *Appl. Surf. Sci.*, 2010, 257(3), 887–898.